INORGANIC CHEMISTRY FRONTIERS

RESEARCH ARTICLE

View Article Online
View Journal | View Issue

Cite this: *Inorg. Chem. Front.*, 2024, **11**, 5273

Fabrication of high-surface-area mesoporous frameworks of β-$Ni(OH)_2$–$CdIn_2S_4$ p–n nano-heterojunctions for improved visible light photocatalytic hydrogen production†

Evangelos K. Andreou, Ioannis Vamvasakis and Gerasimos S. Armatas *

Received 1st May 2024,
Accepted 28th June 2024

DOI: 10.1039/d4qi01092b

rsc.li/frontiers-inorganic

Photocatalytic water splitting holds promise as a cost-effective method for renewable hydrogen production. To this end, synthesising high-performance and robust semiconductor photocatalysts is highly desired. In this study, an interfacial engineering strategy of mesoporous p–n heterojunction frameworks comprising $CdIn_2S_4$ assembled nanocrystals (*ca.* 5–7 nm in size) and β-$Ni(OH)_2$ nanoparticles (*ca.* 7–8 nm in size) with significantly improved photocatalytic hydrogen evolution activity is described. The promotional effect of β-$Ni(OH)_2$ on the electronic band structure and interfacial charge transfer kinetics of heterostructures is systematically elucidated through a combination of spectroscopic and (photo) electrochemical studies. Incorporating β-$Ni(OH)_2$ effectively accelerates the charge separation process and enhances the utilization of surface-reaching photoexcited carriers for redox reactions. Benefiting from the superior charge transfer and mass transport kinetics, the Ni-modified $CdIn_2S_4$ mesostructures release H_2 at a rate of ~20 mmol h^{-1} g_{cat}^{-1} under visible light illumination, corresponding to a 52% apparent quantum efficiency at 420 nm.

Introduction

In recent decades, tremendous research efforts have been made in devising efficient and stable photochemical water-splitting systems for clean energy production.[1–4] Photocatalytic water splitting for hydrogen (H_2) evolution is widely recognized as a promising strategy for replacing the energy supply currently derived from fossil resources.[5–7] This technique offers the advantages of scalability, low operational costs, and minimal carbon footprint, making it an attractive option for widespread adoption. However, to render solar hydrogen production feasible, the development of low-cost and highly efficient semiconductor photocatalysts is imperative. In the past years, a large number of metal oxides (such as TiO_2, $SrTiO_3$, $BiVO_4$, *etc.*), chalcogenides (such as CdS, ZnS, SbS_x, MoS_2, *etc.*) and nitrides (Ta_3N_5, Zn_3N_2, TiN, g-C_3N_4, *etc.*) have been investigated as photocatalytic materials for the hydrogen evolution reaction.[8–15] However, the low photoinduced electron–hole separation efficiency, narrow visible-light absorption (particularly for metal oxide semiconductors) and inadequate photochemical stability (particularly for metal sulfides) still present significant challenges for viable photocatalytic applications.

Spinel sulfide semiconductors have recently emerged as promising catalysts for use in various photo- and electrochemical reactions.[16–18] These compounds, formulated as $A^{II}B_2^{III}S_4$, where A represents a divalent metal ion (such as Zn^{2+}, Cd^{2+}, Ni^{2+} *etc.*) and B represents a trivalent metal ion (such as In^{3+}, Co^{3+}, Fe^{3+}, *etc.*), exhibit high electrical conductivity, multiple redox activities, efficient absorption of the visible light (they have a bandgap of ~2.2–2.6 eV), and exceptional photostability.[19–22] As a result, high-performance thiospinel catalysts, such as $CdIn_2S_4$, $CuCo_2S_4$ and $ZnIn_2S_4$-based materials, have been described for applications in water electrolysis, electrochemical CO_2 reduction and photocatalytic degradation of organic pollutants.[18,20,23] Nevertheless, although promising, the low exposure surface area and competitive electron–hole recombination process seriously limit the hydrogen generation efficiency of these materials. To overcome these obstacles, designing nanoporous semiconductors is an effective strategy for acquiring high-performance photocatalysts.[24] Nanoscale structures could offer a plethora of accessible active sites along with short diffusion pathways for photogenerated carriers, leading to enhanced catalytic activity. Besides, the interfacial engineering strategy to integrate multi-component heterojunctions is also acknowledged as one of the most effective ways to enhance the stability and activity of

Department of Materials Science and Engineering, University of Crete, Vassilika Vouton, Heraklion 70013, Greece. E-mail: garmatas@materials.uoc.gr

† Electronic supplementary information (ESI) available. See DOI: https://doi.org/10.1039/d4qi01092b

the catalyst.[25,26] The heterojunction structure through synergistic interfacial effects between the constituent materials can greatly promote the transfer and separation of photogenerated charge carriers.

We recently described a new synthetic protocol enabling the synthesis of II–III thiospinel colloidal nanocrystals (NCs) and their assembly into mesoporous structures with high porosity and nanoscale pores.[27] Herein, we report the fabrication of highly porous $CdIn_2S_4$ (CIS) nanoarchitectures through the polymer-assisted oxidative coupling of colloidal CIS NCs and their surface modification with β-$Ni(OH)_2$ nanoparticles by using a facile photochemical process. These newly developed materials were investigated as photocatalysts for visible-light-driven hydrogen production, demonstrating exceptional activity and durability. Thorough structural and morphological characterization showed that the Ni-modified CIS materials consist of interconnected small-sized $CdIn_2S_4$ (*ca.* 5–7 nm) and β-$Ni(OH)_2$ (*ca.* 7–8 nm) nanoparticles, forming a 3D porous framework with large internal surface area and uniform mesopores. The charge transfer dynamics and enhanced photocatalytic performance of this system are systematically elucidated by spectroscopic and electrochemical characterization studies. Specifically, the open-pore structure and small grain size composition provide increased accessibility and abundance of catalytically active sites. Moreover, the β-$Ni(OH)_2$ deposition induces efficient separation and better transfer dynamics of photogenerated charge carriers through the formation of p–n β-$Ni(OH)_2$/CIS heterojunctions. Consequently, the Ni-modified sample at 10 wt% Ni content affords a H_2-evolution rate of ~0.4 mmol h^{-1} (or *ca.* 20 mmol h^{-1} g_{cat}^{-1} mass activity) under $\lambda \geq 420$ nm light irradiation with an apparent quantum efficiency (AQE) of 52% at 420 nm.

Results and discussion

Synthesis, structural characterization and morphology

Mesoporous Ni-modified CIS materials were fabricated following a two-step synthesis. Initially, the synthesis of thiol-capped CIS NCs with a diameter of about 6 nm and their integration into porous nanocrystal frameworks (CIS NCFs) were achieved by the method described in a recent study.[27] The synthesis of mesostructures involves the oxidative coupling of colloidal CIS NCs in the presence of a polyoxoethylene-*b*-cetyl ether (Brij-58) block copolymer template. Then, $Ni(OH)_2$ was directly grown on the surface of CIS through the photochemical deposition of a soluble Ni(II) precursor in the presence of triethylamine as a base and sacrificial reagent. As reported, upon light irradiation, the photoexcited electrons of CIS reduce the Ni(II) precursors in the solution, initiating the formation of Ni nanoparticles, which subsequently undergo transformation into Ni$(OH)_2$ in response to the alkaline solution.[28] This is an exceptionally gentle procedure for growing small-sized Ni nanoparticles with uniform distribution and, crucially, in intimate contact with the host surface. The Ni hydroxide on the surface of CIS acts as a hole-transfer mediator to shuttle interfacial hole transport (between the catalyst and electrolyte) and improve the photochemical stability through a synergistic effect among the components. By altering the concentration of the Ni(II) precursor, a series of Ni-modified CIS composites were successfully prepared; denoted as *x*-Ni/CIS NCFs, where *x* represents the mass percentage (wt%) of Ni. The Ni loading in the as-prepared samples was analyzed using energy dispersive spectroscopy (EDS). The EDS spectra of the final products showed the characteristic X-ray peaks of Cd, In, S and Ni (Fig. S1, ESI†), which can be quantified to a Ni content (based on the Ni/Cd atomic ratio) ranging from ~5 to ~15 wt% (Table S1, ESI†). Notably, the measured Ni loadings closely align with the targeted composition of each sample (within 8% deviation), suggesting that all nickel atoms were effectively deposited on the surface of mesoporous CIS.

The X-ray diffraction (XRD) patterns of the prepared materials are shown in Fig. 1a. All the samples showed three broad diffraction peaks within the scattering angles ranging from 20 to 60°, suggesting the existence of small-sized crystalline grains. These diffractions can be attributed to the newly reported hexagonal ($P6_3mc$) crystal phase of $CdIn_2S_4$.[27] Notably, the XRD patterns of Ni/CIS NCFs closely resemble the crystal structure of CIS, with no discernible peaks attributed to Ni species. The absence of Ni XRD peaks is related to the very small grain size and large dispersion of Ni complexes on the surface of CIS. To obtain a clear picture of the crystal structure of the deposited Ni-species, a Ni-modified CIS sample with high Ni content (30 wt%) was also synthesized *via* a similar photochemical deposition process (30-Ni/CIS NCFs) and characterized by XRD. Compared with the pristine CIS, 30-Ni/CIS NCFs exhibited two additional X-ray diffraction peaks at 33° and 59° 2θ scattering angles, which can be assigned to the (100) and (110) reflections of the hexagonal β-$Ni(OH)_2$ (JCPDS card no. 14-0117) (Fig. S2, ESI†). Besides, the atomic configuration of 30-Ni/CIS NCFs was further characterized by X-ray total scattering and pair distribution function analysis (PDF). The PDF analysis can provide information on the local atomic structure of Ni species and CIS host materials.[29] As can be seen in Fig. 1b, the PDF plot of CIS NCFs fully correlates with that of the hexagonal ($P6_3mc$) $CdIn_2S_4$. The distinct interatomic vectors at ~2.5, ~4.0 and ~4.7 Å are M–S (M = Cd/In) bond and M···M nearest and M···S next-nearest-neighbor distances of hexagonal $CdIn_2S_4$, respectively.[27] Compared with mesoporous CIS, the 30-Ni/CIS NCFs sample showed a similar PDF profile, signifying a similar atomic configuration, although some additional correlations in the short-range order (up to 8 Å) can be resolved. The key structural features of the Ni species can be resolved by differential PDF (d-PDF) analysis, which involves subtracting the CIS PDF from that of the 30-Ni/CIS NCFs catalyst. This analysis yields a PDF plot closely resembling that of isolated β-$Ni(OH)_2$ microparticles prepared *via* a simple wet-chemical precipitation process (see the Experimental section for details), offering compelling evidence that the chemical identity of the deposited Ni species is hexagonal β-$Ni(OH)_2$. Specifically, the scattering vector at ~2.1 Å aligns with the Ni–O bond, while those at ~2.6 and ~3.1 Å coincide with the nearest distances of

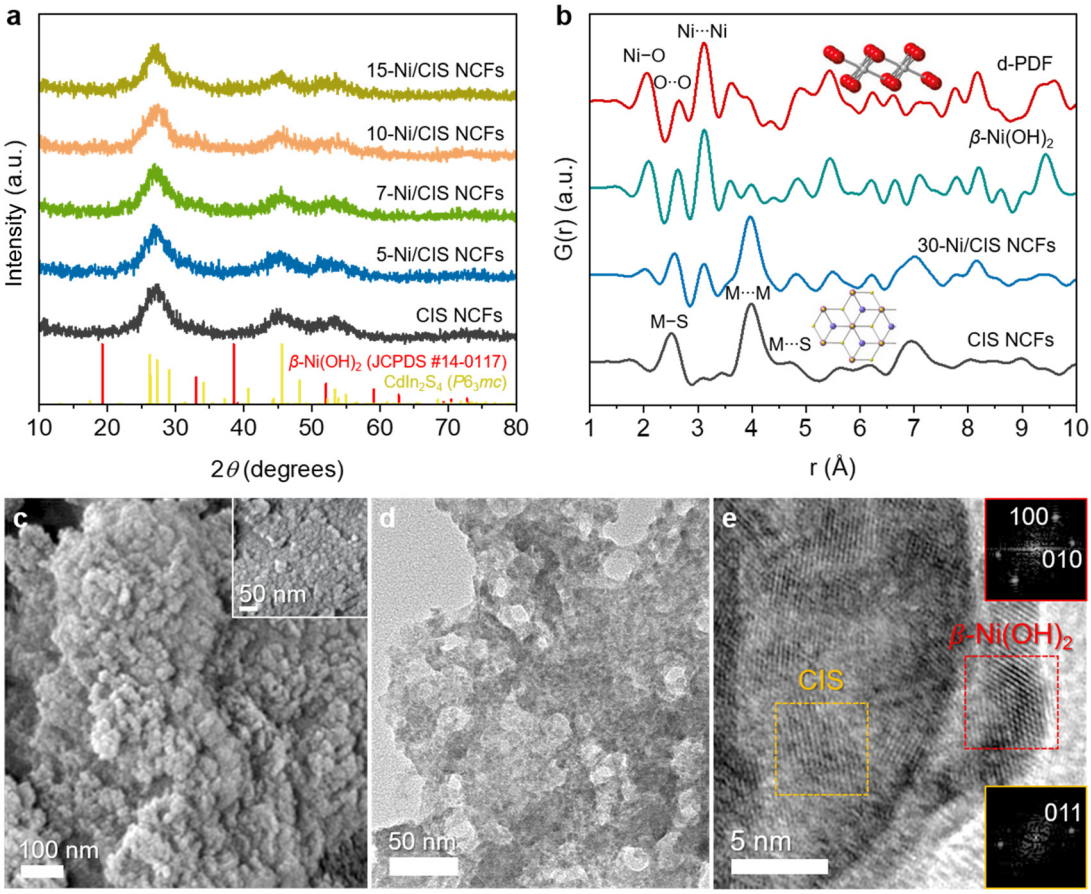

Fig. 1 (a) X-ray diffraction patterns of mesoporous CIS and Ni-modified CIS catalysts. The standard diffraction data of hexagonal $CdIn_2S_4$ and β-$Ni(OH)_2$ (JCPDS card no. 14-0117) are also given. (b) Reduced atomic pair distribution function *G*(*r*) of the mesoporous CIS and 30% Ni-loaded CIS (30-Ni/CIS) NCFs and as-prepared β-$Ni(OH)_2$ microparticles (M = Cd/In). The red line corresponds to the differential PDF (d-PDF) plot obtained by subtracting the CIS PDF from that of 30-Ni/CIS NCFs. (c) Representative FE-SEM (inset: high-magnification image), (d) TEM and (e) high-resolution TEM (HRTEM) images of 10-Ni/CIS NCFs. Inset of panel (e): fast Fourier transform (FFT) patterns indexed to the hexagonal $CdIn_2S_4$ (lattices in the orange frame) and hexagonal β-$Ni(OH)_2$ (lattices in the red frame).

O···O and Ni···Ni in hexagonal β-$Ni(OH)_2$, respectively. These findings reinforce the notion that hexagonal β-$Ni(OH)_2$ crystallites are grown on the surface of CIS NCFs through the photochemical deposition process.

The chemical state of elements in the as-prepared materials was investigated by X-ray photoelectron spectroscopy (XPS). Figs. S3a–d in the ESI† show typical high-resolution XPS spectra of Cd 3d, In 3d, S 2p, Ni 2p and O 1s over the mesoporous CIS and 10-Ni/CIS NCFs, which is the best performing catalyst of this study. Typical XPS spectra obtained from the CIS NCFs display a doublet peak at 405.3 and 412.0 ± 0.2 eV, corresponding to the Cd $3d_{5/2}$ and $3d_{3/2}$ core-levels of Cd^{2+}, and a doublet peak at 444.8 and 452.5 ± 0.2 eV, corresponding to the In $3d_{5/2}$ and $3d_{3/2}$ core-levels of In^{3+} ions in $CdIn_2S_4$, respectively.[30–32] The XPS S 2p spectrum shows a single line at 161.8 ± 0.3 eV, which is attributed to the S^{2-} state. Similarly, the XPS spectra obtained from the 10-Ni/CIS NCFs sample show a doublet peak at 405.2 and 412.0 ± 0.2 eV binding energies in the Cd 3d region due to the Cd $3d_{5/2}$ and $3d_{3/2}$ spin–orbit components of Cd^{2+} ions (Fig. S3a, ESI†), while the peaks at 444.9 and 452.5 ± 0.2 eV in the In 3d region (Fig. S3b, ESI†) are ascribed to the In $3d_{5/2}$ and $3d_{3/2}$ signals of the In^{3+} oxidation state, respectively. Meanwhile, the S 2p peak of the 10-Ni/CIS NCFs at 161.9 ± 0.3 eV agrees well with the S^{2-} valence state, whereas the weak peak at 168.6 ± 0.3 eV is assigned to the inadequate surface oxidation (SO_x species) likely due to the photodeposition process and air exposure of the sample (Fig. S3c, ESI†).[33] The paramagnetic Ni(II) state was further confirmed by the deconvoluted Ni $2p_{3/2}$ and $2p_{1/2}$ subpeaks at 856.1 and 873.9 ± 0.2 eV along with the corresponding satellite peaks at 862.2 and 879.5 ± 0.2 eV (Fig. S3d, ESI†). Consistent with this, the peak at 531.8 ± 0.2 eV and the broad signal at 534.0 ± 0.2 eV in the O 1s region correspond to the hydroxyl groups (Ni–OH) and absorbed moisture (H_2O), respectively (inset of Fig. S3d, ESI†).[28] The XPS analysis revealed a Ni/Cd/In ratio of 1.19 : 1 : 1.98, consistent with a Ni content of ~12.9 wt%, which is comparable to the value obtained by EDS.

Field emission scanning electron microscopy (FESEM) and transmission electron microscopy (TEM) were adopted to

characterize the morphology of the synthesized 10-Ni/CIS NCFs. Typical FESEM images depicted in Fig. 1c display a network structure consisting of aggregated nanoparticles with size smaller than 10 nm. Also, it is evident from the EDS mapping that the Cd, In, S, and Ni elements are distributed uniformly throughout the assembled structure (Fig. S4, ESI†), outlining that β-$Ni(OH)_2$ deposition follows a homogeneous growth on the CIS surface. TEM imaging further confirms the porous morphology of 10-Ni/CIS NCFs, as shown in Fig. 1d. Moreover, high-resolution TEM (HRTEM) indicates that the structure of this sample consists of ~5–7 nm-sized CIS NCs in tight contact with β-$Ni(OH)_2$ nanoparticles of ~7–8 nm diameter (Fig. 1e). This configuration is advantageous for promoting interfacial electronic communication between the components. The structural identification of CIS and β-$Ni(OH)_2$ nanoparticles was further verified by HRTEM analysis. The lattice fringe distances of 3.3 and 2.7 Å seen in Fig. 1e correspond to the (011) planes of hexagonal $CdIn_2S_4$ and the (100) and (010) planes along the [001] zone axis of hexagonal β-$Ni(OH)_2$, respectively. Ultimately, we can conclude that a 3D porous heterostructure comprising β-$Ni(OH)_2$ and CIS NCs in close contact is successfully formed, and it is anticipated to induce enhanced charge carrier delocalization and mass-transfer rates.

N_2 physisorption measurements were performed to investigate the porosity of the prepared materials. Fig. 2a displays the N_2 adsorption–desorption isotherms of mesoporous CIS and 10-Ni/CIS NCFs along with that of bulk CIS microparticles (CIS-m), while the N_2 isotherms of the other Ni-modified samples are presented in Fig. S5 in the ESI.† The mesoporous CIS NCFs exhibited a typical type-IV adsorption isotherm accompanied by an H_2-type hysteresis loop in the desorption branch, being characteristic of mesoporous solids with interconnected pores.[34] Upon modification with β-$Ni(OH)_2$, the resulting materials demonstrated N_2 adsorption–desorption isotherms with an H_3-type hysteresis loop, suggesting a slit-shaped pore morphology. The Brunauer–Emmett–Teller (BET) surface area and pore volume of the mesoporous CIS NCFs were found to be 137 $m^2\ g^{-1}$ and 0.12 $cm^3\ g^{-1}$, respectively. In comparison, CIS microparticles showed limited surface area and pore volume (*ca.* 25 $m^2\ g^{-1}$ and 0.03 $cm^3\ g^{-1}$, respectively), suggesting a non-porous morphology. After β-$Ni(OH)_2$ modification, an increasing trend in the BET surface area (from 137 to 185 $m^2\ g^{-1}$) and pore volume (from 0.165 to 0.23 $cm^3\ g^{-1}$) is observed for the series of Ni/CIS NCFs materials, indicating that the evenly distributed β-$Ni(OH)_2$ layered nanostructures on the surface of CIS NCFs contribute to the overall porosity. The slightly reduced surface area observed in the 15 wt% Ni-loaded sample is likely due to the pore blocking of the CIS support by β-$Ni(OH)_2$ particles. The mean pore size of the samples was determined by applying the non-local density functional theory (NLDFT) model to the adsorption data. All the samples exhibited narrow pore-size distributions (insets of Fig. 2a and Fig. S5, ESI†) with average pore sizes of ~6 nm for CIS NCFs and ~3.6–4.0 nm for the Ni/CIS NCFs, confirming the existence of fairly uniform mesopores in these materials.

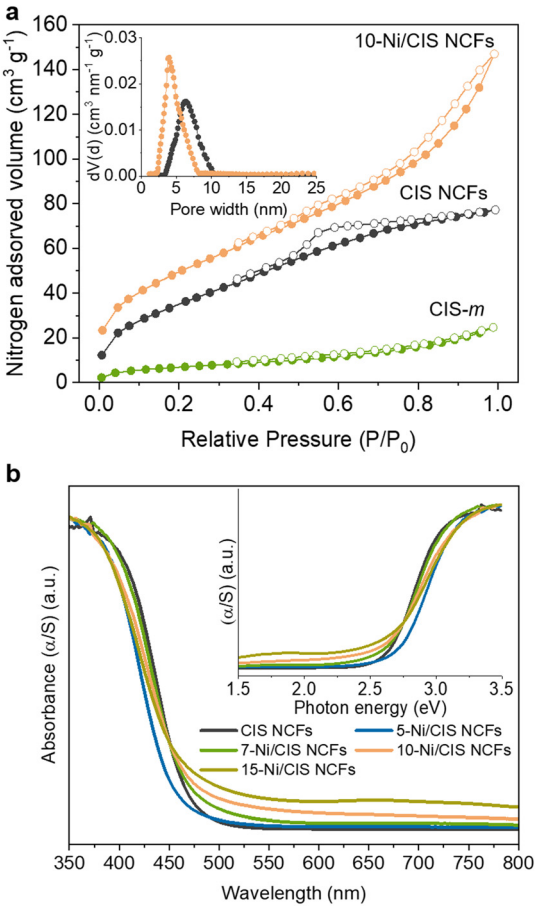

Fig. 2 (a) N_2 adsorption (filled cycles) and desorption (open cycles) isotherms at −196 °C of mesoporous CIS and 10-Ni/CIS NCFs and CIS microparticles (CIS-m). Inset: the corresponding NLDFT pore-size distribution plots calculated from the adsorption isotherms. (b) UV–vis/NIR spectra of mesoporous CIS and Ni-modified CIS NCFs. Inset: the corresponding Kubelka–Munk plots.

Compared to the pristine CIS NCFs, the reduced pore size observed in the Ni-modified samples implies the possible growth of β-$Ni(OH)_2$ nanoclusters within the pores of the CIS material. All the textural parameters for the mesoporous CIS and Ni-modified CIS NCFs are summarized in Table 1.

Ultraviolet–visible/near IR (UV–vis/NIR) diffuse reflectance spectroscopy was employed to investigate the optical properties of the prepared materials. The mesoporous CIS NCFs exhibited a strong absorption onset at 483 nm, which corresponds to the interband electron transition (Fig. 2b). The energy bandgap (E_g) of CIS NCFs, derived from the corresponding Kubelka–Munk plot, was estimated to be 2.57 eV (inset of Fig. 2b). Noteworthily, the energy bandgap of the CIS mesostructure shows a significant blueshift of 0.22 eV compared to the bulk CIS (2.35 eV, Fig. S6, ESI†), probably due to quantization effects in the electronic structure of constituent CIS NCs (*ca.* 5–7 nm in diameter, as determined from TEM analysis). Meanwhile, β-$Ni(OH)_2$ modification of the CIS surface appears to have a considerable effect on the bandgap

Table 1 Textural properties and optical bandgaps of the mesoporous CIS and Ni-modified CIS NCFs and bulk 10 wt% Ni-loaded (10-Ni/CIS-m) sample

Sample	BET surface ($m^2\ g^{-1}$)	Pore volume ($cm^3\ g^{-1}$)	Pore size (nm)	Energy gap[a] (eV)
CIS NCFs	137	0.12	6.3	2.57
5-Ni/CIS NCFs	139	0.17	4.0	2.59
7-Ni/CIS NCFs	156	0.20	3.6	2.52
10-Ni/CIS NCFs	185	0.23	3.9	2.48
15-Ni/CIS NCFs	150	0.20	3.9	2.45
10-Ni/CIS-m	68	0.14	—	2.33

[a] The energy bandgap was obtained from the corresponding Kubelka–Munk plots.

absorption. That is, the E_g of the Ni-modified samples reveals a gradual shift from 2.59 to 2.45 eV as the Ni content increases from 5 to 15 wt% (Table 1). This variation in the energy gap implies strong electronic interactions between the two components within the heterojunction framework. Furthermore, the notable absorption in the visible/near-IR region (wavelength (λ) >550) observed for the Ni/CIS NCFs is attributed to the d–d interband transitions (peaks at ~670 and ~1150 nm) of Ni(II), as inferred from the UV–vis/NIR spectrum of β-Ni$(OH)_2$ microparticles (Fig. S7, ESI†).[35,36] Thus, the above results are entirely consistent with the growth of β-Ni$(OH)_2$ on the surface of CIS NCFs, and more importantly, with strong electronic communication across the interface.

Photocatalytic hydrogen evolution study

The photocatalytic H_2-production activities of different as-prepared materials were evaluated under visible-light irradiation ($\lambda \geq 420$ nm), using triethanolamine (TEOA, 10% v/v) as the sacrificial electron donor. As depicted in Fig. 3a, CIS NCFs exhibited moderate hydrogen evolution activity (~110 μmol h^{-1}), encountering fast charge carrier recombination. Interestingly, modification with β-Ni$(OH)_2$ has a profound promotional effect on the photoactivity of CIS. Even a small amount of β-Ni$(OH)_2$ (5 wt% Ni) induces a ~3 times enhancement of the activity of CIS NCFs, yielding a H_2-evolution rate of 350 μmol h^{-1}. Furthermore, the H_2 generation performance demonstrates a linear response to the Ni content, reaching a maximum of ~395 μmol h^{-1} (or *ca.* 20 mmol h^{-1} g_{cat}^{-1} mass activity) at 10 wt% Ni. An additional increase in the Ni content (up to 15 wt% Ni) results in a notable reduction of the H_2-evolution rate (~320 μmol h^{-1}). We attribute this decline in photoactivity to lower charge-transfer efficiency and increased charge recombination at the β-Ni$(OH)_2$/CIS interface in the highly Ni-loaded sample. The impact of β-Ni$(OH)_2$ hybridization for charge transfer and photoactivity attenuation will be discussed in more detail *via* spectroscopic and electrochemical measurements (see below).

In addition to the compositional effect, the open-pore architecture also plays a significant role in enhancing catalytic activity. To validate this, we prepared a Ni-modified CIS bulk reference sample (denoted as 10-Ni/CIS-m) that has the same Ni content as its mesoporous counterpart (see the Experimental section for details) and measured its H_2-evolution performance under identical conditions. The XRD pattern and EDS spectrum indicated the cubic thiospinel structure and 10.2 wt% Ni composition of 10-Ni/CIS-m (Fig. S8 and Table S1, ESI†), while N_2-physisorption isotherms showed a BET surface area of 68 $m^2\ g^{-1}$ (Fig. S9, ESI,† and Table 1). As shown in Fig. 3a, 10-Ni/CIS-m exhibits significantly lower H_2-evolution activity (~15 μmol h^{-1}) compared to the mesoporous 10-Ni/CIS NCFs, suggesting that the nano-grain composition and large internal surface area are favorable for boosting the photocatalytic performance. Moreover, the effects of different sacrificial electron donors and catalyst concentrations on this photocatalytic system were also investigated through comprehensive control experiments. By keeping a constant catalyst mass loading (1 mg mL^{-1}), irradiation experiments were conducted with various sacrificial donors, such as methanol (MeOH, 10% v/v), ethanol (EtOH, 10% v/v), 5 M NaOH/EtOH mixture (10% v/v), triethylamine (TEA, 10% v/v) and triethanolamine (TEOA, 10% v/v). The significant variations in the rate

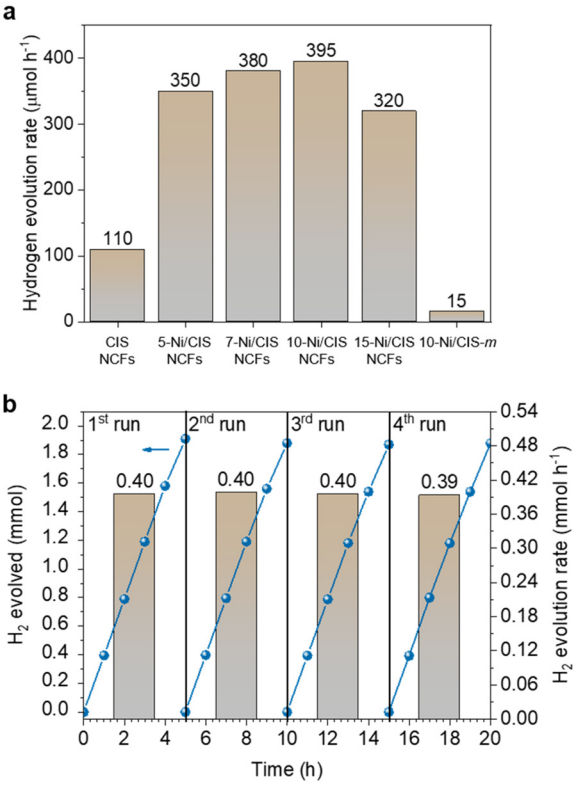

Fig. 3 (a) Hydrogen evolution rates of the mesoporous CIS and Ni-modified CIS NCFs. The H_2-evolution rate of the bulk 10 wt% Ni-loaded CIS (10-Ni/CIS-m) is also given. The rate of H_2 evolution for each catalyst was determined from the average H_2 production over a 3 hour irradiation period. (b) Photocatalytic stability test of the 10-Ni/CIS NCFs. The columns depict the corresponding H_2 evolution rate of each catalytic cycle. Reaction conditions: 1 mg mL^{-1} of catalyst dispersed in aqueous solution containing 10% (v/v) TEOA, 300-W Xe lamp equipped with a UV cut-off filter ($\lambda \geq 420$ nm), 20 ± 2 °C.

of H_2 evolution, as depicted in Fig. S10 in the ESI,† indicate that the oxidation process serves as the rate-limiting step of the overall photocatalytic reaction, while optimal performance is observed when TEOA is used as a sacrificial electron donor. Subsequently, evaluations of photocatalytic performance using different mass loadings of the 10-Ni/CIS NCFs catalyst demonstrated a notable increase in the rate of H_2 evolution with increasing catalyst concentration, reaching a maximum activity at 1 mg mL^{-1} (Fig. S11, ESI†). Further increase in the catalyst amount (>1.5 mg mL^{-1}) led to an abrupt reduction of photocatalytic efficiency by a factor of ~2.3–2.5×. We attribute this decline in performance to increased light scattering caused by the excessive catalyst particles, along with a potential charge attenuation effect due to recombination between adjacent particles. Consequently, under optimized conditions, an apparent quantum efficiency (AQE) of ~52% is obtained at 420 ± 10 nm, considering 100% absorption of the incident photons. To the best of our knowledge, this activity is among the best reported for many $CdIn_2S_4$-based and thiospinel-based photocatalytic systems (Table S2, ESI†). Apart from water reduction, the oxidation of TEOA may also contribute to the overall production of hydrogen.[37] Specifically, TEOA oxidation can yield acetaldehyde (CH_3CHO) and diethanolamine ($HN(CH_2CH_2OH)_2$), where sequential oxidation of these compounds may result in the generation of hydrogen.[38,39] To elucidate this possibility, we further measured the photocatalytic activity for H_2 evolution over 10-Ni/CIS NCFs in the presence of TEOA (10% v/v) and $NaIO_3$ (0.1 M) as the hole and electron scavenger, respectively. Since the reduction of IO_3^- is thermodynamically and kinetically more favorable than water reduction (E° = 1.2 V *versus* 0 V), the photo-reduction of water is negligible in this catalytic system, enabling a focused assessment of potential hydrogen generation *via* the photo-oxidation of TEOA. Interestingly, throughout this reaction, no H_2 gas was detected (by gas chromatography) even after a 3 hour irradiation period, thereby confirming that water is the only hydrogen source.

Moreover, the 10-Ni/CIS NCFs catalyst presents superior photochemical stability, which can be corroborated by the steady rate of hydrogen production throughout recycling experiments. After each catalytic test, the photocatalyst was isolated from the reaction solution through centrifugation, washed with ethanol and water, and then, redispersed in a fresh solution. As displayed in Fig. 3b, 10-Ni/CIS NCFs demonstrated excellent stability even after four 5-hour sequential cycles, where virtually no activity decay was detected. Over the 20 h period, 7.91 mmol (~190 mL at 20 °C) of H_2 is generated, which is equivalent to an average H_2-evolution rate of 0.40 mmol h^{-1}. Moreover, post-reaction EDS, PDF and XPS measurements of the catalyst showed no chemical and structural degradation under the examined conditions (Fig. S12–S14, ESI†). Besides, the N_2 physisorption data of the recycled catalyst were also obtained (Fig. S15, ESI†). Analysis of the adsorption isotherm revealed a slight deterioration in the porous structure, likely attributed to minor photocorrosion and/or nanoparticle rearrangement within the porous framework.

Energy band structure and charge transfer kinetics

The role of β-$Ni(OH)_2$ modification in the charge transfer and separation processes was unraveled by electrochemical spectroscopy. As shown in Fig. 4a, Mott–Schottky plots of the inverse square space-charge capacitance ($1/C_{SC}^2$) as a function of applied voltage (E) were recorded for the mesoporous CIS and Ni-modified CIS NCFs materials [drop-cast on a fluorine-doped tin oxide (FTO, 10 Ω sq^{-1}) substrate]. All the reported electrochemical potentials are presented against the reversible hydrogen electrode (RHE) at pH 7. For mesoporous CIS NCFs, a positive slope of the Mott–Schottky plot is observed, in agreement with its n-type conductivity. In contrast, a bell-shaped $1/C_{SC}^2$–E curve emerges for the Ni-modified samples, which indicates the existence of a p–n junction. As a proof of concept, we have acquired the Mott–Schottky plot of β-$Ni(OH)_2$ microparticles under the same test conditions. In Fig. S16 in the ESI† this sample clearly shows a steep negative gradient of the $1/C_{SC}^2$–E curve, providing direct evidence of the p-type conductivity.[28] As such, the formation of p–n junctions between the p-type β-$Ni(OH)_2$ and n-type CIS NCs undoubtedly dictates the band edge alignment and, thus, the charge transfer and separation processes at the interface. The flat band potential (E_{FB}) of the samples was determined from the intersection point of the Mott–Schottky plots at $1/C_{SC}^2 = 0$. Taking together the calculated E_{FB} potentials and the optical bandgaps (E_g) (as obtained from UV–vis/NIR absorption spectra), the respective conduction (E_C) and valence (E_V) band edge levels for each catalyst can be determined. In this analysis, we assume the E_{FB} potential as a good approximation of the conduction or valence band edge for heavily doped semiconductors; typically, for heavily doped semiconductors, such as the CIS and β-$Ni(OH)_2$, the Fermi level locates within 0.1–0.4 eV from the band edge.[40] All the calculated band-edge potentials are summarized in Table 2 and the corresponding band diagrams of the catalyst are shown in Fig. 4b.

Through this analysis the E_{FB} level for CIS NCFs is obtained as −0.97 V, while deposition of β-$Ni(OH)_2$ significantly changes the E_{FB} position of the Ni/CIS heterostructures. In particular, β-$Ni(OH)_2$ growth on the CIS surface systematically shifts downward the E_{FB} level from −0.70 to −0.50 V. The anodic shift of the E_{FB} position is related to the formation of p–n junctions between the β-$Ni(OH)_2$ and CIS components. Since the Fermi level of β-$Ni(OH)_2$ (~5.2–5.4 eV *vs.* vacuum)[41] is much lower than that of mesoporous CIS (~4.1 eV *vs.* vacuum), an electron flow from CIS to β-$Ni(OH)_2$ nanoparticles will take place upon contact, until their electrochemical potentials align. The net effect of this electron transfer process will decrease the donor concentration (N_D) and generate a potential drop within CIS. Supporting this conclusion, the N_D values for the Ni-modified samples were found to be ~5.5×10^{16}–5.0×10^{17} cm^{-3}, which are lower than that of CIS NCFs (~1.1×10^{18} cm^{-3}), see Table 2. The gradual reduction of N_D affirms the electron transfer from the mesoporous CIS to β-$Ni(OH)_2$ nanoparticles, in agreement with the progressive downshift of the CIS's E_{FB} level. Moreover, compared with mesoporous

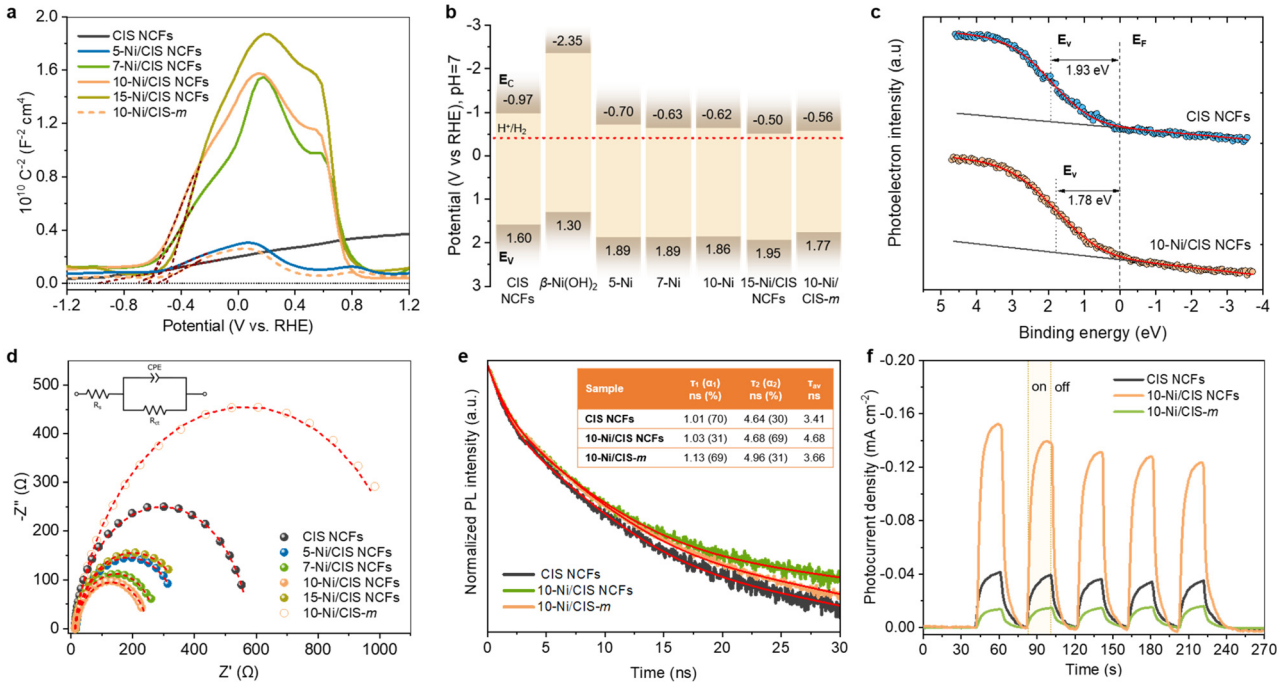

Fig. 4 (a) Mott–Schottky plots measured in a 0.5 M Na_2SO_4 electrolyte (pH = 6.87) using a standard three-electrode cell and (b) energy band diagrams (E_V: valence band energy, E_C: conduction band energy, E_F: Fermi level, and red dashed line: H^+/H_2 redox potential) for the mesoporous CIS and Ni/CIS NCFs and bulk 10-Ni/CIS-m. In panel (b), the band-edge potentials of β-$Ni(OH)_2$ microparticles derived from Mott–Schottky analysis (see Fig. S16, ESI†) are also shown. (c) VB-XPS spectra of the mesoporous CIS and 10-Ni/CIS NCFs. (d) Nyquist plots (Inset: equivalent circuit model used to fit the EIS data) for the mesoporous CIS and Ni/CIS NCFs and bulk 10-Ni/CIS-m. (e) TRPL spectra and (f) transient photocurrent response for the mesoporous CIS and 10-Ni/CIS NCFs and bulk 10-Ni/CIS-m. Inset of panel (e): the PL decay parameters of samples. The average lifetime (τ_{av}) was calculated as $\tau_{av} = \left(\sum_i \alpha_i \tau_i^2\right) / \left(\sum_i \alpha_i \tau_i\right)$ (i = 1, 2). The red lines are fit to the experimental data.

Table 2 Electrochemical data derived through EIS analysis for the mesoporous CIS and Ni/CIS NCFs, and bulk 10-Ni/CIS-m catalysts

Catalyst	E_{FB} (V *vs.* RHE, pH 7)	E_V[a]	Donor concentration (N_D, cm^{-3})	R_{ct} (Ω)
CIS NCFs	−0.97	1.60	1.06×10^{18}	565
5-Ni/CIS NCFs	−0.70	1.89	5.04×10^{17}	346
7-Ni/CIS NCFs	−0.63	1.89	1.17×10^{17}	265
10-Ni/CIS NCFs	−0.62	1.86	8.15×10^{16}	238
15-Ni/CIS NCFs	−0.50	1.95	5.52×10^{16}	373
10-Ni/CIS-m	−0.56	1.77	3.70×10^{17}	1104

[a] The valence band energy (E_V) of the catalysts was estimated from $E_V = E_{FB} + E_g$.

10-Ni/CIS NCFs, the bulk 10-Ni/CIS-m reference sample demonstrated a lower anodic shift of E_{FB} (−0.56 V) and lower N_D concentration loss (~3.7×10^{17} cm^{-3}) relative to the CIS microparticles (E_{FB} ~−0.77 V, N_D ~6.6×10^{17} cm^{-3}, see Fig. S17, ESI†). This implies weak electronic interactions and, thereby, increased interfacial contact resistance between β-Ni$(OH)_2$ and CIS microparticles. Since the position of the Fermi level is affected by the carrier density distribution, it serves as a valuable descriptor for investigating the electron interactions between β-$Ni(OH)_2$ and CIS materials. From the valence band XPS (VB-XPS) spectra, the energy difference of the Fermi level and the E_V of mesoporous CIS and 10-Ni/CIS NCFs was determined to be 1.93 and 1.78 eV, respectively (Fig. 4c). The downshift of the Fermi level upon β-$Ni(OH)_2$ modification clearly confirms an electron injection from CIS to β-$Ni(OH)_2$, as inferred from electrochemical analysis. Thus, we conclude that the changes of the intrinsic CIS band positions induced by β-$Ni(OH)_2$ hybridization are critical factors to improve photocarrier dissociation and transport efficiency.

To further elucidate the effect of β-$Ni(OH)_2$ modification on the charge-transfer dynamics in mesoporous Ni/CIS NCFs, electrochemical impedance spectroscopy (EIS) and photoluminescence (PL) spectroscopy measurements were conducted as well. The EIS Nyquist spectra of various catalysts drop-cast as thin films on FTO electrodes are illustrated in Fig. 4d. A simple equivalent circuit model (inset of Fig. 4d) was used to fit the EIS plots and extract the charge-transfer resistance (R_{ct}) of each catalyst (Table S3, ESI†). The R_{ct} values of the Ni-modified samples (238–373 Ω) revealed much smaller impedance relative to that of pristine CIS NCFs (565 Ω) and isolated β-$Ni(OH)_2$ microparticles (3437 Ω) (Fig. S18, ESI†), which illustrates an improved charge transfer efficiency at the β-$Ni(OH)_2$/CIS contacts; see Table 2. Notably, the declining trend of R_{ct} seen in Table 2 correlates well with the results from the hydrogen production experiments (Fig. 3a), confirming that the charge transfer at the β-$Ni(OH)_2$/CIS contacts is a

rate-limiting factor for the hydrogen evolution reaction. It turns out that the catalyst loaded with 10 wt% Ni (10-Ni/CIS NCFs) possesses the highest charge transfer efficiency (R_{ct} ~238 Ω) among all the as-prepared samples, which agrees well with its superior photocatalytic activity. Interestingly, the bulk reference 10-Ni/CIS-m exhibited a significantly lower charge transport ability (R_{ct} ~1104 Ω) at the catalyst–liquid interface, which is attributed to the poor electronic contact between β-Ni$(OH)_2$ and CIS microparticles, in agreement with our previous EIS results for 10-Ni/CIS-m. Fig. 4e shows the PL decay curves of different catalysts measured under 375 nm pump laser excitation. To depict the kinetic characteristics of the photogenerated charge carriers, the time-resolved PL (TRPL) spectra were properly fitted to a biexponential function: $I(t) = y_0 + \Sigma_i \alpha_i \cdot e^{-t/\tau_i}$ (i = 1, 2), where α_i is the amplitude fraction ($\Sigma_i \alpha_i = 1$) and τ_i is the lifetime for the surface-mediated (τ_1, fast) and intrinsic band-to-band (τ_2, slow) recombination of excitons. Fig. 4e illustrates that the 10-Ni/CIS NCFs exhibit an average electron–hole pair lifetime ~1.3–1.4 times longer (4.68 ns) than the pristine CIS NCFs (3.41 ns) and bulk analogue 10-Ni/CIS-m (3.66 ns), demonstrating the kinetic advantages of the 10-Ni/CIS NCFs for charge transfer. Moreover, by comparing the τ-component fractions of PL decays, we observed a predominant recombination of excitons on the surface of CIS NCFs and 10-Ni/CIS-m; both exhibit a ~69–70% contribution of the fast τ_1-component. In contrast, a significantly lower contribution (~30%) of defect trapping was inferred for mesoporous 10-Ni/CIS NCFs, suggesting lower carrier-recombination loss at the nanostructure interface. Consistent with this, the steady-state PL spectra of mesoporous CIS and 10-Ni/CIS NCFs show an intense PL emission near the band-edge absorption (461 nm, 2.68 eV) of CIS that is notably decreased by β-Ni$(OH)_2$ deposition (Fig. S19, ESI†). This indicates suppressed interband electron–hole relaxation in 10-Ni/CIS NCFs due to the enhanced charge transfer and separation efficiency at the β-Ni$(OH)_2$/CIS interface, in line with the above EIS results. The same conclusions come from transient photocurrent (TPC) measurements. Fig. 4f shows that the mesoporous 10-Ni/CIS NCFs electrode generates a significantly higher photocurrent than the CIS NCFs and 10-Ni/CIS-m electrodes, indicating a more efficient dissociation and migration of photogenerated carriers over the nano-heterostructured catalyst. For example, the 10-Ni/CIS NCFs sample showed a photocurrent density of −0.13 mA cm^{-2} at −1 V *vs.* RHE, while CIS NCFs and 10-Ni/CIS-m showed only −0.04 and −0.02 mA cm^{-2} at the same potential. Evidently, the formation of p–n β-Ni$(OH)_2$/CIS nanoscale junctions triggers an enhanced interfacial charge transfer and separation effect, leading to a more efficient utilization of photoexcited carriers for redox reactions at the catalyst surface.

In light of all the above findings, a band alignment model and charge transfer mechanism for the photocatalytic H_2 evolution reaction over β-Ni$(OH)_2$/CIS mesoporous heterojunctions is proposed in Scheme 1. In particular, β-Ni$(OH)_2$ is a p-type semiconductor with a Fermi level well below that of CIS (~5.2–5.4 eV *vs.* ~4.1 eV) and the close contact between these two components can prompt an electron flow from CIS to β-Ni

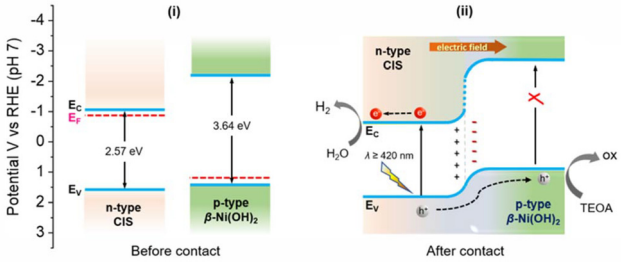

Scheme 1 Energy band diagrams of the n-type CIS and p-type β-Ni$(OH)_2$ semiconductors before (i) and after (ii) contact (E_V: valence band energy, E_C: conduction band energy, and E_F: Fermi level). The band alignment model of the p–n β-Ni$(OH)_2$/CIS junction upon contact illustrates the charge-transfer mechanism of the photocatalytic H_2 evolution by the mesoporous Ni/CIS NCFs.

$(OH)_2$ until the Fermi levels align at the interface.[41] The outcome of this process will create a depletion region, *i.e.*, a positively charged area within CIS, leading to an upward shift in both the E_C and E_V edge potentials near the β-Ni$(OH)_2$/CIS interface. Simultaneously, an accumulation region, *i.e.*, a negatively charged area will develop in the β-Ni$(OH)_2$ side, shifting its band-edges to lower energies.[28] Based on the electrochemical potentials of CIS NCFs (*ca.* 4.1 eV) and β-Ni$(OH)_2$ (*ca.* 5.2–5.4 eV), a significant built-in potential (V_{bi}) of 1.1–1.3 V is expected at the β-Ni$(OH)_2$/CIS interface, resulting in a strong internal electric field directed from CIS to β-Ni$(OH)_2$. It should be stressed that elevating the β-Ni$(OH)_2$ Fermi level upon contact with CIS can effectively diminish the hole transfer barrier of the β-Ni$(OH)_2$/liquid junction, facilitating a more efficient electron collection from the sacrificial donor in solution.[42] The redistribution of charge carriers at the p–n β-Ni$(OH)_2$/CIS heterojunctions is in line with the observations from EIS and VB-XPS analyses. Indeed, all these effects undoubtedly contribute positively to the photocatalytic performance of the Ni/CIS NCFs catalysts. Under visible light illumination, only CIS gets excited and generates electron–hole pairs, as β-Ni$(OH)_2$ does not absorb light within this wavelength range ($\lambda \geq 420$ nm) due to its large bandgap (~3.65 eV). Because of the favorable type-II band scheme (CIS holds more positive E_V and E_C edges compared to β-Ni$(OH)_2$) and the strong electric field in the space-charge layer at the p–n β-Ni$(OH)_2$/CIS junction, the photogenerated holes in the VB of CIS are thermodynamically transferred to β-Ni$(OH)_2$, where they are effectively consumed by the TEOA hole scavenger. This β-Ni$(OH)_2$-mediated hole-transport pathway spatially separates the photogenerated electron–hole pairs, promoting the accumulation of electrons on the CIS surface (mainly on the adjacent Cd and In atoms),[43] where they reduce water and generate hydrogen. This mechanistic model aligns well with the results obtained from EIS, TRPL and TPC studies. Furthermore, benefiting from their highly porous architecture, the Ni/CIS heterostructures provide plenty of surface-active sites and interconnected pore channels for mass transfer, both of which are crucial for improving the efficiency of photo-

catalytic H_2 generation. Supporting evidence for the enhanced electrolyte permeability of 10-Ni/CIS NCFs was obtained through contact angle measurements. The contact angle analysis shown in Fig. S20 in the ESI† indicates a higher diffusion rate and better penetration of water into the mesoporous structure of 10-Ni/CIS NCFs compared to both the pristine CIS NCFs and bulk 10-Ni/CIS-m. Specifically, the water contact angle measures ~14° for 10-Ni/CIS NCFs, ~20° for CIS NCFs and ~30° for 10-Ni/CIS-m after diffusion for 400 ms. This confirms that both Ni modification and open-pore configuration are essential features of the Ni/CIS NCFs for enhancing the wettability of the catalyst, thereby increasing the water–catalyst interface area.

Conclusions

In this work, mesoporous frameworks of linked β-$Ni(OH)_2$-modified $CdIn_2S_4$ nanocrystals were successfully prepared by a polymer-templated chemical method, followed by a photochemical deposition process. Characterization through UV–vis/NIR, electrochemical impedance and photoluminescence spectroscopy techniques revealed that Ni modification effectively tunes the kinetics of charge transfer and separation, leading to a significantly enhanced photocatalytic performance for hydrogen evolution. The p-type β-$Ni(OH)_2$ nanoparticles serve as efficient hole-transport mediators, facilitating the transfer of photogenerated holes from the n-type $CdIn_2S_4$ photocatalyst to the oxidant. Moreover, the pertinent mesoporous architecture of these materials provides enhanced exposure of active sites for reactions and facilitates rapid electrolyte transport between the nanoparticles. Consequently, the catalyst containing 10 wt% Ni exhibits exceptional photocatalytic activity and stability for the hydrogen evolution reaction, yielding a H_2 evolution rate of ~0.4 mmol h^{-1} (or *ca.* 20 mmol h^{-1} g_{cat}^{-1} mass activity) under $\lambda \geq 420$ nm light irradiation with an apparent quantum efficiency of 52% at 420 nm. This work opens up a new pathway for designing and comprehensively understanding highly efficient multicomponent semiconductor p–n junctions for viable solar-to-chemical energy conversion.

Experimental section

Synthesis of mesoporous CIS NCFs

The mesoporous $CdIn_2S_4$ nanocrystal frameworks (CIS NCFs) were synthesized following a previously reported protocol.[27] For a typical synthesis of colloidal CIS NCs, 50 mL of ethanediol solution containing $Cd(NO_3)_2$, $In(NO_3)_2$ and 3-mercaptopropionic acid (3-MPA) (molar ratio 1 : 2 : 24) were inserted in a double-neck flask and heated under reflux conditions at 150 °C in an oil bath. When the solution reached 150 °C, 10 mL of an ethanediol solution containing thioacetamide (8 mmol) was injected into the flask, and the resulting mixture was left to react under mild stirring for 6 h. The 3-MPA-capped CIS NCs (~5 nm in size) were isolated with isopropanol/centrifugation and drying at 40 °C overnight. For the preparation of the mesoporous structures, 250 mg of CIS NCs were dispersed in 2.5 mL of DI water of pH ~9 (adjusted using a few drops of NH_4OH solution). When a colloidal suspension was formed, 2.5 mL of a Brij-58 aqueous solution (~10% w/w) were added to the suspension, and the mixture was stirred for 1 h at room temperature. Next, the oxidative polymerization of the sulfide NCs was initiated with the addition of 1.2 mL of diluted H_2O_2 (3% v/v) solution. After gelation for about 30 min at room temperature, the sample was transferred to a furnace and kept at 40 °C for 2–3 days to evaporate the solvent. The final mesoporous material (CIS NCFs) was obtained after removal of the polymer-template through several washing cycles with DI water and ethanol, using vacuum filtration, and drying at 60 °C for 12 h.

Also, for comparison purposes, a bulk material of $CdIn_2S_4$ microparticles (CIS-m) was synthesized following a similar reflux synthetic procedure at 150 °C but without the addition of a capping agent (3-MPA).

Photodeposition of β-$Ni(OH)_2$ on CIS NCFs

The photodeposition of β-$Ni(OH)_2$ on the surface of mesoporous CIS NCFs was performed by the following procedure. Briefly, 100 mg of the CIS NCFs were dispersed by ultrasonication in 20 mL aqueous solution containing 10% (v/v) triethylamine (TEA). Then, an appropriate aliquot of the $NiCl_2{\cdot}6H_2O$ aqueous solution (1 mg mL^{-1}), corresponding to a desired mass loading of Ni from 5 to 15 wt%, was added to the above dispersion under continuous stirring at room temperature. Before irradiation, the resulting mixture was sealed in an airtight custom-made Pyrex reactor and purged with Ar gas for 30 min. Next, the reaction mixture was illuminated for 1.5 h using a 375 nm light-emitting diode (50-W LED) as the light source. The final product was then collected through centrifugation, washed several times with deionized (DI) water and ethanol, and dried at 60 °C for 12 h. Through this procedure, a series of Ni-modified CIS NCF samples with different loading amounts of Ni was prepared (denoted as *x*-Ni/CIS NCFs, where x = 5, 7, 10 and 15 wt% of Ni content).

For comparative studies, a control sample denoted as 10-Ni/CIS-m was also synthesized by photochemical deposition of 10 wt% Ni on bulk CIS microparticles. In addition, bulk β-$Ni(OH)_2$ microparticles were synthesized following a chemical precipitation method. In particular, 10 mL of a 4 M NaOH solution were mixed with a $NiCl_2$ solution (1 M, 10 mL) to form a light-green dispersion. The mixture was left at 60 °C for 24 h under continuous stirring, and the final product was collected by centrifugation, washed several times with DI water and ethanol, and dried at 60 °C for 12 h.

Physicochemical characterization

The chemical composition and surface morphology were examined with a JEOL JSM-IT700HR field emission scanning electron microscope (FESEM) equipped with an energy-dispersive spectrometer (EDS). EDS data of each sample were acquired from at least ten different locations using an acceler-

ating voltage of 20 kV and a 60 s accumulation time. Transmission electron microscopy (TEM) imaging was conducted on a JEOL JEM-2100 microscope using a 200 kV accelerating voltage (LaB_6 filament). X-ray diffraction measurements were performed on a Panalytical X'pert Pro MPD diffractometer using Cu-Kα radiation (λ = 1.5418 Å), operating at 45 kV and 40 mA. X-ray diffuse scattering measurements were conducted using a Bruker D8 Venture diffractometer equipped with a PHOTON II CPAD detector at room temperature. Data were collected in capillary transmission geometry using a Mo-Kα source (λ = 0.7093 Å). The diffraction data were corrected for empty cell scattering. The X-ray total scattering data [$I(q) = f(q)$, where q (=$4\pi \sin\theta/\lambda$) is the wavevector] were Fourier transformed to obtain the pair distribution function (PDF) plots using PDFgetX3.[44] X-ray photoelectron spectroscopy (XPS) spectra were recorded using a SPECs spectrometer equipped with a Phoibos 100 1D-DLD electron analyzer and a monochromated Al-Kα line (1486.6 eV) as the X-ray source. All the reported XPS spectra were corrected with respect to the adventitious carbon C 1s peak at 284.8 eV. N_2 physisorption measurements were performed on a Quantachrome NOVA 3200*e* sorption analyzer at −196 °C. Prior to each measurement, the samples were degassed at 100 °C for at least 12 h. The specific surface areas were calculated using the Brunauer–Emmett–Teller (BET) method[45] at the relative pressure (P/P_0) range of 0.04–0.24. The total pore volume of the samples was estimated from the N_2 adsorption at P/P_0 = 0.98. The pore-size distribution plots were obtained by applying the non-local density functional theory (NLDFT) model to fit the adsorption data.[46] UV–vis/NIR diffuse reflectance spectroscopy was conducted on a Shimadzu UV-2600 spectrophotometer using $BaSO_4$ as a 100% reflectance reference and as a substrate for the samples. The Kubelka–Munk function was used to transform the diffuse reflectance data to the respective absorbance: $\alpha/S = (1 - R)^2/(2R)$, where R is the measured reflectance, and α and S are the absorption and scattering coefficients, respectively. The time-resolved photoluminescence (TRPL) spectra were acquired at room temperature using an Edinburgh FS5 spectrofluorometer. A pulsed blue laser (375 nm, 50 ns pulses) was used as the excitation source. TRPL spectra of the mesoporous CIS and 10-Ni/CIS NCFs were recorded at an emission wavelength of 468 nm, while that of bulk 10-Ni/CIS-m was recorded at 545 nm emission.

Photocatalytic hydrogen evolution reactions

Photocatalytic H_2 evolution experiments were performed using a custom-made Pyrex-glass reactor sealed airtight. For a typical experiment, 20 mg of photocatalyst were first dispersed *via* ultrasonication for 5 min in a 20 mL water/triethanolamine (TEOA) solution (9 : 1 v/v) until a uniform suspension was formed. Then, the photocatalytic reactor was sealed and the reaction mixture underwent deaeration for 30 minutes through Ar gas purging. In order to maintain a stable temperature (20 ± 2 °C) throughout all experiments, the reactor was immersed in a water-bath cooling system during light irradiation. The light source employed (300-W xenon lamp, Variac Cermax) was equipped with a UV cut-off filter (Asahi Techno Glass) allowing only visible-light wavelengths ($\lambda \geq 420$ nm) to pass through. The amount of hydrogen gas evolved was determined using a gas chromatographer (GC) equipped with a TCD detector (Shimadzu GC-2014, Ar carrier gas).

The apparent quantum efficiency (AQE) was obtained by dividing the amount of evolved H_2 by the intensity of incident light at λ = 420 ± 10 nm monochromatic light using the following equation:

$$\mathrm{AQE}(\%) = \frac{2^* N_{H_2}}{N_{hv}} \times 100\% \quad (1)$$

where, N_{H2} and N_{hv} account for the number of H_2 molecules evolved and number of incident photons, respectively. The intensity of incident light was measured using a StarLite radiometer coupled with a calibrated FL400A-BB-50 thermal detector (Ophir Optronics Ltd) and was found to be 7 mW cm^{-2}, corresponding to the number of incident photons of about 1.48×10^{16} per second.

Photoelectrochemical measurements

The electrochemical properties of the prepared samples were investigated using a Princeton Applied Research potentiostat/EIS workstation model VersaSTAT 4. A three-electrode cell composed of a sample-coated fluorine-doped tin oxide (FTO, 10 Ω sq^{-1}) working electrode, a Ag/AgCl (saturated KCl) reference electrode, and a Pt counter electrode, was used. The working electrode was prepared as follows: 10 mg of each sample were dispersed in 1 mL of ethanol by ultrasonication to form a uniform suspension. Next, 500 μL of the sample "ink" were drop-cast on the conductive surface of a clean FTO glass substrate (effective area: 1 cm^2) and dried at 60 °C for 1 h to form a stable film. The Mott–Schottky plots were obtained by measuring the space-charge capacitance (C_{SC}) of the working electrodes in a 0.5 M $NaSO_4$ electrolyte (pH = 6.87) at a frequency of 1 kHz using a 10 mV AC voltage amplitude. All the measured potentials in the Ag/AgCl scale were converted to the reversible hydrogen electrode (RHE) scale using the following equation:

$$E_{RHE} = E_{Ag/AgCl} + 0.197\ \mathrm{V}\ (\text{at } 25°\mathrm{C}) \quad (2)$$

where, E_{RHE} refers to the potential in the RHE scale and $E_{Ag/AgCl}$ is the measured potential in the Ag/AgCl scale.

Using the Mott–Schottky equation, the donor concentration (N_D) of samples was calculated using the equation below.

$$N_D = 2 \cdot (E - E_{FB}) \cdot {C_{SC}}^2/(\varepsilon \cdot \varepsilon_0 \cdot e_0) \quad (3)$$

where, C_{SC} is the space-charge capacitance, E is the applied voltage, E_{FB} is the flat-band potential, N_D is the donor concentration, ε is the dielectric permittivity of the semiconductor material (6.6 for $CdIn_2S_4$),[47] ε_0 is the vacuum permittivity (8.8542×10^{-14} F cm^{-1}), and e_0 is the elementary charge (1.602×10^{-19} C).

The Nyquist plots were collected in the frequency range of 1 Hz to 100 kHz using an applied DC bias of −1.0 V *vs.* Ag/AgCl

(saturated KCl). The experimental EIS data were fitted using ZView software to an equivalent Randles circuit model, consisting of an electrolyte resistance (R_s), a charge-transfer resistance (R_{ct}) and a constant phase element (CPE) that accounts for the non-ideal capacitance response. Transient photocurrent curves were recorded under chopped visible-light irradiation ($\lambda \geq 420$ nm) at a fixed bias of −1 V (*vs.* Ag/AgCl) in a 0.5 M Na_2SO_4 electrolyte.

Author contributions

All authors contributed to the design of the experiments, the interpretation of the results and a discussion of the outline of the manuscript. E.K.A. performed the materials' synthesis, physicochemical characterization and catalytic activity studies. Dr I.V. performed the electrochemical measurements. G.S.A. supervised the process and wrote the manuscript with input from all the authors. All authors approved the final version of the manuscript.

Data availability

The data supporting this article have been included as part of the ESI.†

Conflicts of interest

There are no conflicts to declare.

Acknowledgements

This study was carried out within the framework of the National Recovery and Resilience Plan Greece 2.0 (Award Number TAEDR-0535821), funded by the European Union – NextGenerationEU. E. K. A. gratefully acknowledges financial support from the Special Account for Research Funds of University of Crete (SARF UOC) (KA 11203). The open access publishing of this article is financially supported by HEAL-Link.

References

1 W. Wang, J. M. Herreros, A. Tsolakis and A. P. E. York, Reducing CO_2 footprint through synergies in carbon free energy vectors and low carbon fuels, *Energy*, 2016, **112**, 976–983.
2 M. Yu, K. Wang and H. Vredenburg, Insights into low-carbon hydrogen production methods: Green, blue and aqua hydrogen, *Int. J. Hydrogen Energy*, 2021, **46**, 21261–21273.
3 N. Z. Muradov and T. N. Veziroğlu, "Green" path from fossil-based to hydrogen economy: An overview of carbon-neutral technologies, *Int. J. Hydrogen Energy*, 2008, **33**, 6804–6839.
4 G. Chehade and I. Dincer, Progress in green ammonia production as potential carbon-free fuel, *Fuel*, 2021, **299**, 120845.
5 S. Nishioka, F. E. Osterloh, X. Wang, T. E. Mallouk and K. Maeda, Photocatalytic water splitting, *Nat. Rev. Methods Primers*, 2023, **3**, 1–15.
6 C. Acar, I. Dincer and G. F. Naterer, Review of photocatalytic water-splitting methods for sustainable hydrogen production, *Int. J. Energy Res.*, 2016, **40**, 1449–1473.
7 X. Liu, X. Zhang, D.-S. Li, S. Zhang and Q. Zhang, Recent advances in the "on-off" approaches for on-demand liquid-phase hydrogen evolution, *J. Mater. Chem. A*, 2021, **9**, 1449–1473.
8 S. Chandrasekaran, L. Yao, L. Deng, C. Bowen, Y. Zhang, S. Chen, Z. Lin, F. Peng and P. Zhang, Recent advances in metal sulfides: from controlled fabrication to electrocatalytic, photocatalytic and photoelectrochemical water splitting and beyond, *Chem. Soc. Rev.*, 2019, **48**, 4178–4280.
9 K. Maeda, Photocatalytic water splitting using semiconductor particles: History and recent developments, *J. Photochem. Photobiol., C*, 2011, **12**, 237–268.
10 F. E. Osterloh, Inorganic nanostructures for photoelectrochemical and photocatalytic water splitting, *Chem. Soc. Rev.*, 2013, **42**, 2294–2320.
11 M. Rahman, H. Tian and T. Edvinsson, Revisiting the limiting factors for overall water-splitting on organic photocatalysts, *Angew. Chem.*, 2020, **132**, 16418–16433.
12 I. Tamiolakis, I. T. Papadas, K. C. Spyridopoulos and G. S. Armatas, Mesoporous assembled structures of Cu_2O and TiO_2 nanoparticles for highly efficient photocatalytic hydrogen generation from water, *RSC Adv.*, 2016, **6**, 54848–54855.
13 I. Tamiolakis, D. Liu, F. X. Xiao, J. Xie, I. T. Papadas, T. Salim, B. Liu, Q. Zhang, S. A. Choulis and G. S. Armatas, Mesoporous implantable Pt/$SrTiO_3$:C,N nanocuboids delivering enhanced photocatalytic H_2-production activity via plasmon-induced interfacial electron transfer, *Appl. Catal., B*, 2018, **236**, 338–347.
14 Z. Cheng, W. Qi, C. H. Pang, T. Thomas, T. Wu, S. Liu and M. Yang, Recent advances in transition metal nitride-based materials for photocatalytic applications, *Adv. Funct. Mater.*, 2021, **31**, 2100553.
15 Y. Liu, P. D. Kanhere, C. L. Wong, Y. Tian, Y. Feng, F. Boey, T. Wu, H. Chen, T. J. White, Z. Chen and Q. Zhang, Hydrazine-hydrothermal method to synthesize three-dimensional chalcogenide framework for photocatalytic hydrogen generation, *J. Solid State Chem.*, 2010, **183**, 2644–2649.
16 F. Ozel, H. S. Kilic, H. Coskun, I. Deveci, A. Sarilmaz, A. Balikcioglu, Y. Gundogdu, A. Aljabour, A. Ozen, S. Y. Gezgin, A. Houimi, A. Yar, M. Kus and M. Ersoz, A general review on the thiospinels and their energy applications, *Mater. Today Energy*, 2021, **21**, 100822.
17 G. Zhang, H. Wu, D. Chen, N. Li, Q. Xu, H. Li, J. He and J. Lu, A mini-review on $ZnIn_2S_4$-Based photocatalysts for

energy and environmental application, *Green Energy Environ.*, 2022, **7**, 176–204.
18 R. Yang, L. Mei, Y. Fan, Q. Zhang, R. Zhu, R. Amal, Z. Yin and Z. Zeng, $ZnIn_2S_4$-Based Photocatalysts for Energy and Environmental Applications, *Small Methods*, 2021, **5**, 2100887.
19 X. Shi, C. Dai, X. Wang, J. Hu, J. Zhang, L. Zheng, L. Mao, H. Zheng and M. Zhu, Protruding Pt single-sites on hexagonal $ZnIn_2S_4$ to accelerate photocatalytic hydrogen evolution, *Nat. Commun.*, 2022, **13**, 1–10.
20 S. Bra, I. Vamvasakis, E. K. Andreou, G. Vailakis, G. Kopidakis and G. S. Armatas, Modulating interfacial charge redistribution of $Ni_2P/CuCo_2S_4$ p–n nano-heterojunctions for efficient electrocatalytic overall water splitting, *Int. J. Hydrogen Energy*, 2023, **48**, 25300–25314.
21 Y. Wu, X. Liu, D. Han, X. Song, L. Shi, Y. Song, S. Niu, Y. Xie, J. Cai, S. Wu, J. Kang, J. Zhou, Z. Chen, X. Zheng, X. Xiao and G. Wang, Electron density modulation of $NiCo_2S_4$ nanowires by nitrogen incorporation for highly efficient hydrogen evolution catalysis, *Nat. Commun.*, 2018, **9**, 1–9.
22 B. B. Kale, J. O. Baeg, S. M. Lee, H. Chang, S. J. Moon and C. W. Lee, $CdIn_2S_4$ Nanotubes and "marigold" nanostructures: A visible-light photocatalyst, *Adv. Funct. Mater.*, 2006, **16**, 1349–1354.
23 S. Wang, B. Y. Guan, Y. Lu and X. W. Lou, Formation of hierarchical In_2S_3–$CdIn_2S_4$ heterostructured nanotubes for efficient and stable visible light CO_2 reduction, *J. Am. Chem. Soc.*, 2017, **139**, 17305–17308.
24 T. D. C. Ha, H. Lee, I. Vamvasakis, G. S. Armatas, Y. Oh and M. G. Kim, Recent developments in porous metal chalcogenides for environmental remediation and sustainable energy, *EcoMat*, 2023, e12419.
25 H. Wang, L. Zhang, Z. Chen, J. Hu, S. Li, Z. Wang, J. Liu and X. Wang, Semiconductor heterojunction photocatalysts: design, construction, and photocatalytic performances, *Chem. Soc. Rev.*, 2014, **43**, 5234–5244.
26 J. Low, J. Yu, M. Jaroniec, S. Wageh and A. A. Al-Ghamdi, Heterojunction photocatalysts, *Adv. Mater.*, 2017, **29**, 1601694.
27 E. K. Andreou, I. Vamvasakis and G. S. Armatas, High-performance mesoporous catalysts of ultrasmall hexagonal thiospinel nanocrystals for visible–light hydrogen evolution, *Adv. Mater. Interfaces*, 2024, **11**, 2300994.
28 I. Vamvasakis, I. T. Papadas, T. Tzanoudakis, C. Drivas, S. A. Choulis, S. Kennou and G. S. Armatas, Visible-light photocatalytic H_2 production activity of β-$Ni(OH)_2$-modified CdS mesoporous nanoheterojunction networks, *ACS Catal.*, 2018, **8**, 8726–8738.
29 S. J. L. Billinge and M. G. Kanatzidis, Beyond Crystallography: The study of disorder, nanocrystallinity and crystallographically challenged materials with pair distribution functions, *Chem. Commun.*, 2004, **4**, 749–760.
30 W. Zhang, H. Yang, W. Fu, M. Li, Y. Li and W. Yu, Directly hydrothermal growth of $CdIn_2S_4$ nanosheet films on FTO substrates for photoelectric application, *J. Alloys Compd.*, 2013, **561**, 10–15.
31 X. Ma, W. Li, H. Li, M. Dong, L. Geng, T. Wang, H. Zhou, Y. Li and M. Li, Novel noble-metal-free $Co_2P/CdIn_2S_4$ heterojunction photocatalysts for elevated photocatalytic H_2 production: Light absorption, charge separation and active site, *J. Colloid Interface Sci.*, 2023, **639**, 87–95.
32 W. Chen, T. Huang, Y. X. Hua, T. Y. Liu, X. H. Liu and S. M. Chen, Hierarchical $CdIn_2S_4$ microspheres wrapped by mesoporous g-C_3N_4 ultrathin nanosheets with enhanced visible light driven photocatalytic reduction activity, *J. Hazard. Mater.*, 2016, **320**, 529–538.
33 M. Sun, X. Zhao, Q. Zeng, T. Yan, P. Ji, T. Wu, D. Wei and B. Du, Facile synthesis of hierarchical $ZnIn_2S_4/CdIn_2S_4$ microspheres with enhanced visible light driven photocatalytic activity, *Appl. Surf. Sci.*, 2017, **407**, 328–336.
34 J. Rouquerol, F. Rouquerol, P. Llewellyn, G. Maurin and K. S. W. Sing, *Adsorption by Powders and Porous Solids: Principles, Methodology and Applications*, 2nd edn, 2013, pp. 1–626.
35 D. S. Hall, D. J. Lockwood, C. Bock and B. R. MacDougall, Nickel hydroxides and related materials: A review of their structures, synthesis and properties, *Proc. R. Soc. A*, 2015, **471**, 20140792.
36 K. Ikeda and S. Vedanand, Optical spectrum of synthetic theophrastite $Ni(OH)_2$, *Neues Jahrb. Mineral., Monatsh.*, 1999, **1**, 21–26.
37 F. Costantino and P. V. Kamat, Do sacrificial donors donate H_2 in photocatalysis?, *ACS Energy Lett.*, 2022, **7**, 242–246.
38 J. Schneider and D. W. Bahnemann, Undesired role of sacrificial reagents in photocatalysis, *J. Phys. Chem. Lett.*, 2013, **4**, 3479–3483.
39 P. V. Kamat and S. Jin, Semiconductor photocatalysis: "Tell us the complete story!", *ACS Energy Lett.*, 2018, **3**, 622–623.
40 Z. Zhang and J. T. Yates, Band bending in semiconductors: Chemical and physical consequences at surfaces and interfaces, *Chem. Rev.*, 2012, **112**, 5520–5551.
41 I. A. Digdaya, G. W. P. Adhyaksa, B. J. Trzesniewski, E. C. Garnett and W. A. Smith, Interfacial engineering of metal-insulator-semiconductor junctions for efficient and stable photoelectrochemical water oxidation, *Nat. Commun.*, 2017, **8**, 1–8.
42 K. Becker, C. Xiao, S. Assavachin, A. Kundmann and F. E. Osterloh, 14.8% Quantum efficient gallium phosphide photocatalyst for hydrogen evolution, *J. Am. Chem. Soc.*, 2024, **146**, 7723–7733.
43 H. Wang, Y. Xia, H. Li, X. Wang, Y. Yu, X. Jiao and D. Chen, Highly active deficient ternary sulfide photoanode for photoelectrochemical water splitting, *Nat. Commun.*, 2020, **11**, 1–11.
44 P. Juhás, T. Davis, C. L. Farrow and S. J. L. Billinge, PDFgetX3: A rapid and highly automatable program for processing powder diffraction data into total scattering pair distribution functions, *J. Appl. Crystallogr.*, 2013, **46**, 560–566.
45 S. Brunauer, L. S. Deming, W. E. Deming and E. Teller, On a theory of the van der Waals adsorption of gases, *J. Am. Chem. Soc.*, 1940, **62**, 1723–1732.

46 P. I. Ravikovitch, D. Wei, W. T. Chueh, G. L. Haller and A. V. Neimark, Evaluation of pore structure parameters of MCM-41 catalyst supports and catalysts by means of nitrogen and argon adsorption, *J. Phys. Chem. B*, 1997, **101**, 3671–3679.

47 R. R. Sawant, K. Y. Rajpure and C. H. Bhosale, Determination of $CdIn_2S_4$ semiconductor parameters by (photo) electrochemical technique, *Phys. B*, 2007, **393**, 249–254.